Simulation of Quantum Transport in Monolithic ICs Based on $In_{0.53}Ga_{0.47}As$–$In_{0.52}Al_{0.48}As$ RTDs and HEMTs With a Quantum Hydrodynamic Transport Model

Jan Höntschel, Roland Stenzel, *Member, IEEE*, and Wilfried Klix

***Abstract*—A new quantum hydrodynamic transport model based on a quantum fluid model is used for numerical calculations of different quantum sized devices. The simulation of monolithic integrated circuits of resonant tunneling structures and high electron mobility transistors (HEMT) based on $In_{053}Ga_{0.47}As$–$In_{052}Al_{0.48}As$–InP is demonstrated. With the new model, it is possible to describe quantum mechanical transport phenomena like resonant tunneling of carriers through potential barriers and particle accumulation in quantum wells. Different structure variations, especially the resonant tunneling diode area and the gate width of the HEMT structure, show variable modulations in the output characteristics of the monolithic integrated device.**

***Index Terms*—Device simulation, high electron mobility transistors (HEMTs), quantum hydrodynamic, quantum transport, resonant tunneling devices.**

I. Introduction

CIRCUITS THAT use resonant tunneling diodes (RTDs) hold promise as a technology for ultradense high-speed integrated digital logic devices. The negative differential resistance of the current–voltage (*I–V*) characteristic in RTDs can be used to reduce device counts per circuit functions, thus increasing circuit integration density [1]. The very fast switching capability makes them suitable for high-speed circuits. High electron mobility transistors (HEMTs) integrated with RTDs reduce power consumption, due to the gain and high input to output isolations provided by the transistors. In particular, these devices are attractive for applications in new computing architectures such as neuronal networks and cellular automata, in which even a simple function requires a large number of conventional transistors due to limited functionality.

For the simulation of the complex nanoscale semiconductor devices, it is necessary to include quantum mechanical transport phenomena, like tunneling processes of carriers through potential barriers or particle accumulation in quantum wells in the physical model. The quantum hydrodynamic simulation, which is based on a quantum fluid dynamic model offers expanding possibilities for the understanding as well as the design of such novel quantum sized semiconductor devices. The advantage of this model is its macroscopic character, because a description without knowledge of quantum mechanical details like initial wave function is obtained. The derivation of the full three-dimensional quantum hydrodynamic transport model, based on the Wigner–Boltzmann equation with a shifted moment expansion, delivers the same conservation law as the classical conversation law, but the energy density and the energy balance equation as well as the stress tensor have additional quantum terms [2]. The consequence of these additional quantum terms is the extension of the classical hydrodynamic model for the semiconductor device simulation by expressions in the transport, and in the energy balance equations, which describe an internal quantum potential in the transport equation as well as a quantum heat flux in the energy balance equation. These additional terms in the classical hydrodynamic model allow us to describe a continuous electron and hole distribution in a semiconductor device, accumulations of carriers in potential wells and resonant tunneling of carriers, respectively.

In [24]–[28] the derivation of the quantum hydrodynamic model based on the Schrödinger equation by a quasi-classical approach is described. It delivers the same quantum hydrodynamic model equations and shows the connection to the quantum hydrodynamic model, which is derived from the Wigner–Boltzmann equation.

Numerical investigations of MESFETs and HEMTs based on GaAs–AlGaAs material system by using quantum moment equations are described in [29]–[31]. Simulations of RTD structures with a quantum drift diffusion model and the quantum moment balance equations are presented in [32] and [33]. Other approaches for the modeling of quantum devices are, for instance, Wigner function methods [38], [39] and density matrix methods [40].

Microscopic/macroscopic models, which are based on the self-consistent one-dimensional or two-dimensional (2-D) solution of the Schrödinger and Poisson equation, depending on the confinement of electrons, deliver a continuity description of the electron density distribution from the initial wave function as well, but they do not include tunneling processes [17]. The main problem in the microscopic device simulation is the computation time. To decrease the simulation time the microscopic

Manuscript received April 27, 2003; revised January 22, 2004. This work was supported by the German Federal Ministry of Education, Science, Research and Technology under Contract 01 BM 911. The review of this paper was arranged by Editor S. Datta.

The authors are with the Department of Electrical Engineering, University of Applied Sciences Dresden, D-01069 Dresden, Germany (e-mail: hoentsch@et.htw-dresden.de).

Digital Object Identifier 10.1109/TED.2004.825815

model of Schrödinger and Poisson equation is only applied in the parts of the device where electron gases appear and it is coupled with the known macroscopic drift diffusion model for all other parts. But with a quantum hydrodynamic description it is possible to take into account quantum mechanical effects in all directions of a total complex nanometer structure at acceptable computation times.

This paper describes the first reported numerical simulation of monolithic integrated circuits (ICs) of resonant tunneling structures and HEMTs based on $In_{0.53}Ga_{0.47}As$–$In_{0.52}Al_{0.48}As$–InP with a novel quantum hydrodynamic model. Section II shows the derivation and the properties of the appropriate quantum flux model. The survey of the numerical algorithm of the quantum hydrodynamic model follows after the summary of the quantum transport models. Section IV presents the numerical results and the discussion of different structure variations, especially the gate width (W_G) and the RTD area (A_{RTD}), of the simulated monolithic integrated device.

II. Quantum Transport Models

A. Quantum Hydrodynamic Model

The derivation of the quantum hydrodynamic transport model is based on a shifted moment expansion with the Wigner–Boltzmann transport [2]. The time expansion of the Wigner distribution function

$$f_W(\boldsymbol{R},\boldsymbol{p},t)=\frac{1}{(2\pi\hbar)^3}\int_{-\infty}^{\infty}\Psi\left(\boldsymbol{R}+\frac{\boldsymbol{r}}{2},t\right)\Psi^*\left(\boldsymbol{R}-\frac{\boldsymbol{r}}{2},t\right)\exp\left(-\frac{i}{\hbar}\boldsymbol{p}\cdot\boldsymbol{r}\right)d^3\boldsymbol{r} \quad (1)$$

which is the Fourier transform of the density matrix for a mixed state by using the Schrödinger equation delivers the collision-less Wigner–Boltzmann transport equation or Quantum–Lioville equation [3]

$$\left[\frac{\partial}{\partial t}+\frac{\boldsymbol{p}}{m_n}\nabla_{\boldsymbol{R}}-\nabla_{\boldsymbol{R}}V(\boldsymbol{R},t)\cdot\nabla_{\boldsymbol{p}}\right]f_W(\boldsymbol{R},\boldsymbol{p},t)+\frac{\hbar^2}{4}\sum_{k+l+m=3}\frac{\partial^3V(\boldsymbol{R},t)}{\partial R_1^k\partial R_2^l\partial R_3^m}\frac{1}{k!l!m!}\frac{\partial^3 f_W(\boldsymbol{R},\boldsymbol{p},t)}{\partial p_1^k\partial p_2^l\partial p_3^m}=0. \quad (2)$$

$\boldsymbol{R}$ denotes the center of mass coordinate, and $\boldsymbol{r}$ is the separation vector. m_n describes the effective mass of the occupation probability of the carrier, and $\boldsymbol{p}$ is the moment. The quantum correction of the Wigner–Boltzmann equation is proportional to $\hbar^2$ and disappears for potentials, which mostly depend on quadratic coordinates of $\boldsymbol{R}$. For this particular case, the classical Lioville equation is reproduced. The second term of (2) describes diffusion, and the third one, drift processes. Terms with derivations of third order in $\boldsymbol{R}$ of the Wigner–Boltzmann transport equation is an expression of nonlocality in quantum mechanics, which is a consequence of the Heisenberg relation.

The conservation law of the Wigner–Boltzmann equation (2) delivers the same results as the classical conservation law for the average expectation values of the moments [4]. The shifted average moments of the Wigner distribution functions are determined in [5].

The first conservation law delivers the continuity equation with the first moment

$$\nabla_{\boldsymbol{R}}\cdot\boldsymbol{j}_n(\boldsymbol{R},t)=e\left(R-G+\frac{\partial n(\boldsymbol{R},t)}{\partial t}\right). \quad (3)$$

The second conservation law, which the first and second shifted moments and the continuity equation (3) are included in, describes the transport equation

$$\begin{aligned}&\boldsymbol{j}_n(\boldsymbol{R},t)+\tau_{\boldsymbol{p},n}n(\boldsymbol{R},t)\frac{\partial}{\partial t}\left(\frac{\boldsymbol{j}_n(\boldsymbol{R},t)}{n(\boldsymbol{R},t)}\right)\\&-\frac{\tau_{\boldsymbol{p},n}}{e}(\boldsymbol{j}_n(\boldsymbol{R},t)\cdot\nabla_{\boldsymbol{R}})\cdot\left(\frac{\boldsymbol{j}_n(\boldsymbol{R},t)}{n(\boldsymbol{R},t)}\right)\\&=-e\mu_n n(\boldsymbol{R},t)\nabla_{\boldsymbol{R}}\varphi(\boldsymbol{R},t)\\&-e\mu_n n(\boldsymbol{R},t)\nabla_{\boldsymbol{R}}\left(-\frac{k_B}{e}T_n(\boldsymbol{R},t)\right)+eD_n\nabla_{\boldsymbol{R}}(n(\boldsymbol{R},t))\\&-2\cdot\frac{\mu_n\hbar^2}{4dm_n}n(\boldsymbol{R},t)\nabla_{\boldsymbol{R}}\left(\frac{\Delta_{\boldsymbol{R}}\sqrt{n(\boldsymbol{R},t)}}{\sqrt{n(\boldsymbol{R},t)}}\right).\end{aligned} \quad (4)$$

The treatment of the average velocity and the temperature tensor in the quadratic term of the second conversation law is the same as the classical derivation of the hydrodynamic transport model [4].

The quantum correction term is interpreted as the nondiagonal quantum stress tensor

$$\hat{\boldsymbol{p}}_q\Big(n(\boldsymbol{R},t)\Big)=-\frac{\hbar^2}{4m_n}n(\boldsymbol{R},t)\left[\nabla^2_{\boldsymbol{R}}\left(\ln\Big(n(\boldsymbol{R},t)\Big)\right)\right] \quad (5)$$

or as self-internal quantum energy, the so-called Bohm potential [6], [18]–[20]

$$Q\Big(n(\boldsymbol{R},t)\Big)=-\frac{\hbar^2}{2m_n}\frac{\Delta_{\boldsymbol{R}}\sqrt{n(\boldsymbol{R},t)}}{\sqrt{n(\boldsymbol{R},t)}}. \quad (6)$$

The divergence of the quantum correction term in the second shifted moment of the Wigner density distribution function delivers the density gradient term in the transport equation

$$n(\boldsymbol{R},t)\nabla_{\boldsymbol{R}}\left(\frac{\Delta_{\boldsymbol{R}}\sqrt{n(\boldsymbol{R},t)}}{\sqrt{n(\boldsymbol{R},t)}}\right)=\frac{1}{2}\nabla_{\boldsymbol{R}}\cdot\left[n(\boldsymbol{R},t)\nabla^2_{\boldsymbol{R}}\left(\ln\Big(n(\boldsymbol{R},t)\Big)\right)\right]. \quad (7)$$

For the confinement of an electron system in the quantum correction term of (4) the parameter d is included, which is a value between 2 and 3.

The derivation of the energy balance equation, the energy flux density, and the energy density for the quantum hydrodynamic model is based on the third conversation law and the shifted moments of the Wigner distribution function. The relation between the average carrier velocity and the conductivity heat flux density is used in the same way as in the derivation of the classical hydrodynamic model [4]. So the energy balance equation is

$$\begin{aligned}&\frac{\partial}{\partial t}(n(\boldsymbol{R},t)\langle w_n\rangle)+\nabla_{\boldsymbol{R}}\cdot\boldsymbol{S}_n(\boldsymbol{R},t)-\boldsymbol{j}_n(\boldsymbol{R},t)\cdot\boldsymbol{E}(\boldsymbol{R},t)\\&-\frac{\hbar^2}{8dm_ne}\nabla_{\boldsymbol{R}}\cdot\left[n(\boldsymbol{R},t)\nabla^2_{\boldsymbol{R}}\left(\frac{\boldsymbol{j}_n(\boldsymbol{R},t)}{n(\boldsymbol{R},t)}\right)\right]\\&=-n(\boldsymbol{R},t)\frac{\langle w_n\rangle-\langle w_n\rangle_{\mathrm{equal}}}{\tau_{E,n}}+\langle w_n\rangle(G-R)\end{aligned} \quad (8)$$

where the energy flux density

$$\boldsymbol{S}_n(\boldsymbol{R},t) = -\kappa_n \nabla_{\boldsymbol{R}} T_n(\boldsymbol{R},t) - \frac{1}{e}\left[\langle w_n\rangle + k_B T_n(\boldsymbol{R},t) - \frac{\hbar^2}{4dm_n}\nabla^2_{\boldsymbol{R}}[\ln\Big(n(\boldsymbol{R},t)\Big)]\right]\boldsymbol{j}_n(\boldsymbol{R},t) \quad (9)$$

and the energy density

$$\langle w_n\rangle = \frac{m_n}{2}\boldsymbol{v}(\boldsymbol{R},t)^2 + \frac{3}{2}k_B T_n(\boldsymbol{R},t) - \frac{\hbar^2}{8dm_n}\Delta_{\boldsymbol{R}}\Big[\ln\Big(n(\boldsymbol{R},t)\Big)\Big] \quad (10)$$

are included. The quantum correction term in the energy balance equation (8) is the so-called quantum heat flux term, which was derived in [15], [16], and [20]. The parameter d is also included in the quantum correction terms of the energy conservation equations (8)–(10).

B. Quantum Energy Balance Model

The classical hydrodynamic model can be truncated to the computationally faster energy transport model while including basically the same physics for most semiconductor devices. Investigations of practical applications show that the relations in the transport equation (4), where the impulse relaxation time $\tau_{\boldsymbol{p},n}$ is included, the quantum heat flux term in the energy balance equation (8) and the average kinetic energy in the equation for the energy density (10) can be neglected. The quantum hydrodynamic model can be reduced to the quantum energy balance model with the continuity equation (3), the transport equation

$$\boldsymbol{j}_n(\boldsymbol{R},t) = -e\mu_n n(\boldsymbol{R},t)\nabla_{\boldsymbol{R}}\left(\varphi(\boldsymbol{R},t) - \frac{k_B}{e}T_n(\boldsymbol{R},t)\right) + eD_n\nabla_{\boldsymbol{R}}\Big(n(\boldsymbol{R},t)\Big) - 2\cdot\frac{\mu_n\hbar^2}{4\,d\,m_n}n(\boldsymbol{R},t)\nabla_{\boldsymbol{R}}\left(\frac{\Delta_{\boldsymbol{R}}\sqrt{n(\boldsymbol{R},t)}}{\sqrt{n(\boldsymbol{R},t)}}\right) \quad (11)$$

the energy balance equation

$$\begin{aligned}\nabla_{\boldsymbol{R}}\cdot\boldsymbol{S}_n(\boldsymbol{R},t) &= \boldsymbol{j}_n(\boldsymbol{R},t)\cdot\boldsymbol{E}(\boldsymbol{R},t)\\ &- \frac{3}{2}k_B\frac{\partial}{\partial t}\Big(n(\boldsymbol{R},t)T_n(\boldsymbol{R},t)\Big)\\ &- \frac{3k_B}{2\tau_{E,n}}n(\boldsymbol{R},t)\Big(T_n(\boldsymbol{R},t) - T_L\Big)\\ &+ \frac{3}{2}k_B T_n(\boldsymbol{R},t)(G-R)\\ &+ \frac{\hbar^2}{8dm_n}\Delta_{\boldsymbol{R}}\Big[\ln\Big(n(\boldsymbol{R},t)\Big)\Big]\left[\frac{n(\boldsymbol{R},t)}{\tau_{E,n}} - (G-R)\right]\\ &+ \frac{\hbar^2}{8\,d\,m_n}\frac{\partial}{\partial t}n(\boldsymbol{R},t)\Delta_{\boldsymbol{R}}\Big[\ln\Big(n(\boldsymbol{R},t)\Big)\Big] \end{aligned} \quad (12)$$

where the energy density with the quantum correction term is included and the corresponding energy flux density is

$$\boldsymbol{S}_n(\boldsymbol{R},t) = -\kappa_n\nabla_{\boldsymbol{R}}T_n(\boldsymbol{R},t) - \frac{1}{e}\left[\frac{5}{2}k_B T_n(\boldsymbol{R},t) - \frac{3}{2}\frac{\hbar^2}{4dm_n}\nabla^2_{\boldsymbol{R}}[\ln\Big(n(\boldsymbol{R},t)\Big)]\right]\boldsymbol{j}_n(\boldsymbol{R},t). \quad (13)$$

The parameter κ_n in (9) and (13) for the energy flux density of both quantum hydrodynamic transport models denotes the carrier heat conductivity and is described by the Wiedemann–Franz law.

C. Quantum Drift Diffusion Model

The quantum drift diffusion transport model or density gradient transport model is deduced from the quantum energy balance model with the assumption that the electrical field in the vicinity of the semiconductor device is unfluctuated. Furthermore, the carrier temperature is equal to the lattice temperature. Based on these suppositions, the solution of the energy conversation equations (12), (13) is negligible. The carrier temperature gradient in the transport equation (11) comes to zero. The quantum drift diffusion transport model is reduced to the continuity equation (3) and the quantum drift diffusion transport equation is

$$\boldsymbol{j}_n(\boldsymbol{R},t) = -e\mu_n n(\boldsymbol{R},t)\nabla_{\boldsymbol{R}}\varphi(\boldsymbol{R},t) + eD_n\nabla_{\boldsymbol{R}}n(\boldsymbol{R},t) - 2\cdot\frac{\mu_n\hbar^2}{4dm_n}n(\boldsymbol{R},t)\nabla_{\boldsymbol{R}}\left(\frac{\Delta_{\boldsymbol{R}}\sqrt{n(\boldsymbol{R},t)}}{\sqrt{n(\boldsymbol{R},t)}}\right) \quad (14)$$

where the density gradient term is included. The quantum drift diffusion model or the so-called density gradient model is used to describe the behavior of electrons in the vicinity of strong inversion layers near the gate oxide of MOS transistors [22], [23], [34] or as a quantum correction for the classical drift diffusion equations [35]–[37].

The classical hydrodynamic transport model, the classical energy balance transport model, and the standard drift diffusion transport model can be received if $\hbar^2 \to 0$ is in the transport and energy balance equations as well as in the equations for the energy density and energy flux density.

III. Implementation and Numerical Aspects

For the numerical implementations of the quantum hydrodynamic model an approach of the quantum energy balance model is used, where the quantum correction terms in the different transport equations (11)–(13) are an expression of a quantum correction potential, similar to Wettstein *et al.* [12]. Especially the approach

$$2\frac{\Delta_{\boldsymbol{R}}\sqrt{n(\boldsymbol{R},t)}}{\sqrt{n(\boldsymbol{R},t)}} \approx \Delta_{\boldsymbol{R}}\Big[\ln(n(\boldsymbol{R},t))\Big] \approx \nabla^2_{\boldsymbol{R}}\Big[\ln\Big(n(\boldsymbol{R},t)\Big)\Big] \quad (15)$$

is introduced. The quantum hydrodynamic model, which is applied for the numerical simulation can be expressed in the Poisson equation

$$\nabla_{\boldsymbol{R}}\cdot(\varepsilon\nabla_{\boldsymbol{R}}\varphi(\boldsymbol{R},t)) = -e\Big[p(\boldsymbol{R},t) - n(\boldsymbol{R},t) + N_D^+ - N_A^-\Big] \quad (16)$$

the continuity equation

$$\nabla_{\boldsymbol{R}}\cdot\boldsymbol{j}_n(\boldsymbol{R},t) = e\left(R - G + \frac{\partial n(\boldsymbol{R},t)}{\partial t}\right) \quad (17)$$

the quantum correction potential

$$\lambda_n(\boldsymbol{R},t) = 2\cdot\frac{\gamma_n\hbar^2}{12m_n e}\frac{\Delta_{\boldsymbol{R}}\sqrt{n(\boldsymbol{R},t)}}{\sqrt{n(\boldsymbol{R},t)}} \quad (18)$$

the transport equation

$$\boldsymbol{j}_n(\boldsymbol{R},t) = +eD_n\nabla_{\boldsymbol{R}}n(\boldsymbol{R},t) - e\mu_n n(\boldsymbol{R},t) \nabla_{\boldsymbol{R}}\left(\varphi(\boldsymbol{R},t) - \frac{k_B}{e}T_n(\boldsymbol{R},t) + \lambda_n(\boldsymbol{R},t) + \Theta_n\right) \quad (19)$$

the energy balance equation

$$\begin{aligned}&\nabla_{\boldsymbol{R}}\cdot\boldsymbol{S}_n(\boldsymbol{R},t)\\ &-\frac{3}{2}k_BT_n(\boldsymbol{R},t)(G-R) = \boldsymbol{j}_n(\boldsymbol{R},t)\cdot\boldsymbol{E}(\boldsymbol{R},t)\\ &-\frac{3}{2}k_B\frac{\partial}{\partial t}n(\boldsymbol{R},t)T_n(\boldsymbol{R},t) - \frac{3k_B}{2\tau_{E,n}}n(\boldsymbol{R},t)(T_n(\boldsymbol{R},t)-T_L)\\ &+\frac{1}{2}e\lambda_n(\boldsymbol{R},t)\left[\frac{n(\boldsymbol{R},t)}{\tau_{E,n}} - (G-R)\right]\\ &+\frac{1}{2}e\frac{\partial}{\partial t}n(\boldsymbol{R},t)\lambda_n(\boldsymbol{R},t) \qquad (20)\end{aligned}$$

and the energy flux density

$$\boldsymbol{S}_n(\boldsymbol{R},t) = -\kappa_n\nabla_{\boldsymbol{R}}T_n(\boldsymbol{R},t) - \frac{5}{2}\frac{k_B}{e}T_n(\boldsymbol{R},t)\boldsymbol{j}_n(\boldsymbol{R},t) + \frac{3}{2}\lambda_n(\boldsymbol{R},t)\boldsymbol{j}_n(\boldsymbol{R},t). \quad (21)$$

For the parameter d in the quantum correction potential the value 3 is used.

The problem of the anisotropic effective mass is handled by the fitting factor γ_n, which is a calibration factor for the influence of quantum mechanical effects on the conventional carrier transport [12]. The quantum correction potential in the drift gradient of the transport equation (11) and in the energy balance equation (12), as well as the energy flux density (13) is included. The so-called band parameter Θ_n is inserted in the drift gradient of the transport equation (11) to simulate device structures with different materials.

The energy relaxation time $\tau_{E,n}$ in the energy balance equation (12) is calculated by a modified model [7]

$$\tau_{E,n} = \tau_{\boldsymbol{p},n,0}\frac{T_L}{T_n(\boldsymbol{R},t)}\left(1+\frac{3\,k_BT_n(\boldsymbol{R},t)}{c_nm_nv_{s,n}^2}\right). \quad (22)$$

$\tau_{\boldsymbol{p},n,0}$ denotes the impulse relaxation time, $v_{s,n}$ is the saturation velocity of the carriers, and c_n is a calibration parameter.

Numerical investigations of RTD structures, where the results of the quantum hydrodynamic model are compared to the results of the transfer matrix method, and to measurement data show the possibility of the calibration of the tunneling peak current by the energy relaxation time model [21].

Implementations of the quantum hydrodynamic model using finite element and finite difference methods are reported in [2], [8], [9] and [12]. The device simulation environment SIMBA used for the numerical calculations is based on the finite box method [10] and [11].

The approach for $\lambda_n(\boldsymbol{R},t)$ as a new variable increases the number of unknown variables of the nonlinear system. On the other hand, as (18) is only of second order, it can be discretized conventionally by combining function values with the nearest neighboring grid points only.

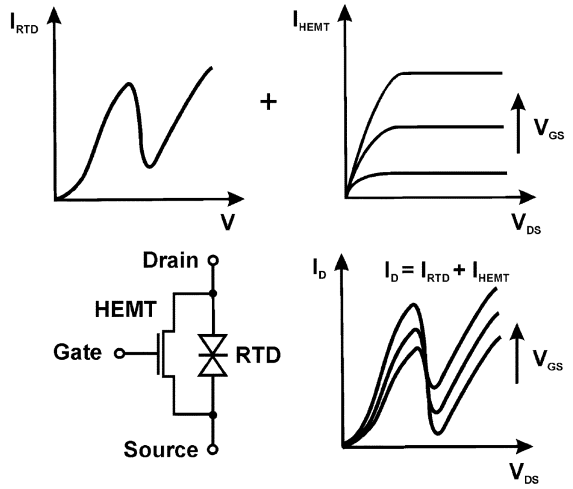

Fig. 1. Schematics and modulation scheme for the peak current, which is based on the parallel integration of RTD and HEMT [14]. The total drain current I_D is the sum of the currents through the RTD and HEMT.

For (17) and (19)–(21), the Scharfetter–Gummel discretization [13] is used. The quantum correction potential (18) is discretized as

$$\Omega^i\lambda_n^i = \frac{\gamma_n\hbar^2}{6m_ne}\sum_j\left[\frac{\sigma^{i,j}}{l^{i,j}}\left(\exp\left[\frac{\Phi_C^j+\varphi^j+\lambda_n^j}{2k_BT^j/e} - \frac{\Phi_C^i+\varphi^i+\lambda_n^i}{2k_BT^i/e}\right]-1\right)\right]. \quad (23)$$

The indexes i and j are used to designate grid points. The j-sum covers the nearest neighbors of grid point i. Ω^i is the volume of the box for grid point i, $l^{i,j}$ is the distance of grid points i and j, and $\sigma^{i,j}$ is the normal area of the box between these points. As boundary conditions for (23), $\nabla_{\boldsymbol{R}}(\Phi_C+\varphi+\lambda_n)=0$ at the device boundaries are assumed. This corresponds to $\nabla_{\boldsymbol{R}}n(\boldsymbol{R},t)=0$ for the density-based formula (18) at the discretization of the quantum correction potential.

Equation (23) is solved by a damped Newton iteration, which is used for the calculation of the Poisson equation. The total coupled system of the quantum hydrodynamic model is calculated by the Gummel algorithm.

IV. Simulation Results

A. Device Structure

The operating principle of an integrated RTD-HEMT pair is represented in Fig. 1. Experimental investigations of such structures are shown in [14], which are applied for high performance monostable bistable transition logic elements.

In the integrated device, a HEMT is connected in parallel to an RTD. The total drain current (I_D) is equal to the sum of the current passing through the RTD (I_{RTD}) and the HEMT (I_{HEMT}). Since the gate source voltage (V_{GS}) can modulate I_{HEMT}, I_D is also modulated by V_{GS}. As a result, the peak current of the integrated device is modulated by V_{GS}. It should be noted that the resonant tunneling current through the RTD remains unchanged at different gate biases. The cross section of the device structure, which was used for the simulations,

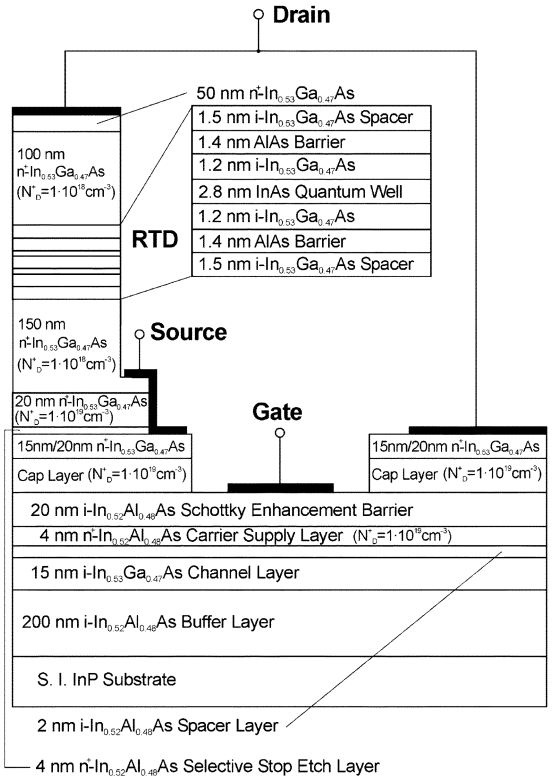

Fig. 2. Schematic cross section of the simulated monolithic integrated RTD-HEMT device.

is represented in Fig. 2 together with the doping densities as well as the layer thicknesses. For the numerical investigations some assumptions are imported. The contact areas of the drain and source are highly doped regions with a density of $N_D = 1.0 \cdot 10^{19}$ cm^{-3} to ensure the channel connection of the HEMT. The metal contact of the source is turned around to the bottom of the device structure, connecting the highly doped areas. The S.I.–InP substrate and the selective etch stop layer is neglected for the simulation, because the main carrier transport is concentrated in the channel of the HEMT and in the RTD structure. For the simulations with the quantum hydrodynamic model, the relaxation time model (22) is applied. Two different relaxation times $\tau_{\boldsymbol{p},n}$ and calibration parameters c_n in the model (22) are used, where $\tau_{\boldsymbol{p},n} = 1.0$ fs and $c_n = 22$ for the $In_{0.53}Ga_{0.47}As$–AlAs–InAs material system is meant for the range of the RTD, and $\tau_{\boldsymbol{p},n} = 2.8$ ps and $c_n = 2.2$ for the $In_{0.53}Ga_{0.47}As$–$In_{0.52}Al_{0.48}As$–InP material system for the area of the HEMT.

B. Device Characteristics

At first an integrated device, which has an RTD area of $A_{\mathrm{RTD}} = 5.0\ \mu$m^2 and a gate width of $W_G = 10.0\ \mu$m as well as a gate length of $L_G = 700$ nm is investigated. The calculated operating principle of the parallel connection of the RTD and a HEMT is represented in the output characteristics (Fig. 3). The drain current of the IC is equal to the sum of the current through the RTD (I_{RTD}) and the drain current through the HEMT (I_{HEMT}). The isolated RTD exhibits a peak to valley ratio of $P/V = 4.5$ at a temperature of $T = 300$ K, with a peak-current density of $J_{\mathrm{peak}} = 1.5 \cdot 10^5$ A/cm^2. The isolated HEMT delivers a maximum transconductance of $g_{m,\max} = 850$ mS/mm with a threshold voltage $V_{\mathrm{th}} = -0.47$ V for the 700-nm gate length device. The calculated characteristics of the RTD and HEMT are comparable to the reported values for the InP-based material system. It should be noted that the current flow through the single HEMT device for $V_{\mathrm{GS}} = 0$ and $V_{\mathrm{DS}} = 0.31$ V (peak voltage) is $I_D = 2.14$ mA and for $V_{\mathrm{DS}} = 0.34$ V (valley voltage) is $I_D = 2.19$ mA, which results in the reduced peak-to-valley ratio of $P/V = 2.5$ at zero gate bias.

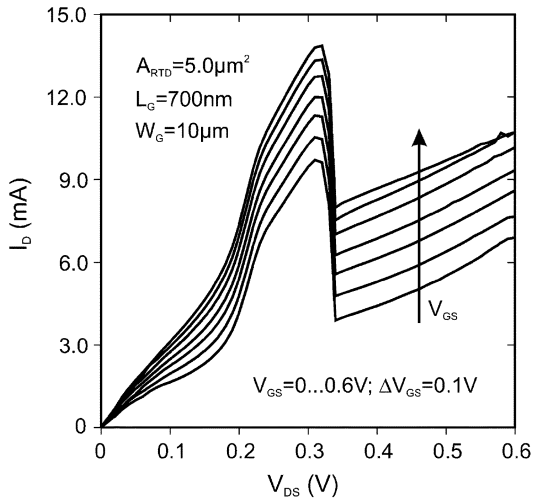

Fig. 3. Output characteristics of the IC.

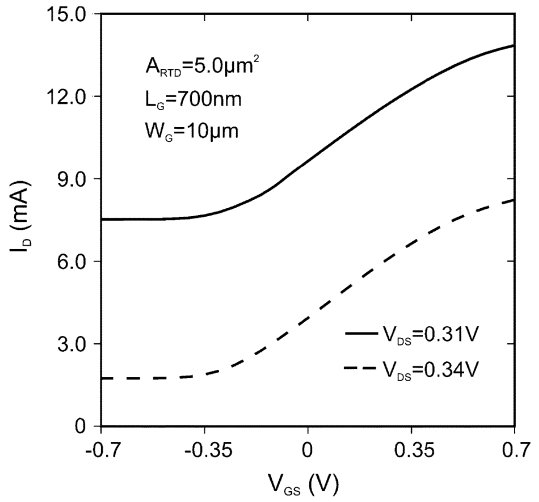

Fig. 4. Transfer characteristics of the RTD-HEMT structure.

Fig. 4 shows the transfer characteristics at different drain–source voltages of the integrated parallel connection of the RTD and HEMT. As expected, an increase of the drain current at lower drain–source voltages can be detected.

The electron density distributions at $V_{\mathrm{DS,peak}}$ and $V_{\mathrm{DS,valley}}$ are represented in Fig. 5 only for the integrated RTD. A carrier accumulation in the quantum well at the peak voltage is obtained. The increase of the electron density between the potential barriers at $V_{\mathrm{DS,peak}}$ is caused by the tunnel processes through the RTD. The accumulation region of electrons, where the carriers tunnel into the potential well from, can be recognized. The depletion region, which the electrons tunnel into from the potential well, can be observed behind the potential

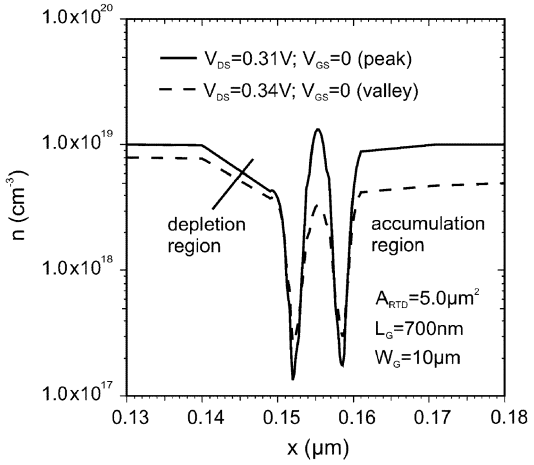

Fig. 5. Electron density distribution at $V_{\mathrm{DS,peak}}$ and $V_{\mathrm{DS,valley}}$ for the integrated RTD.

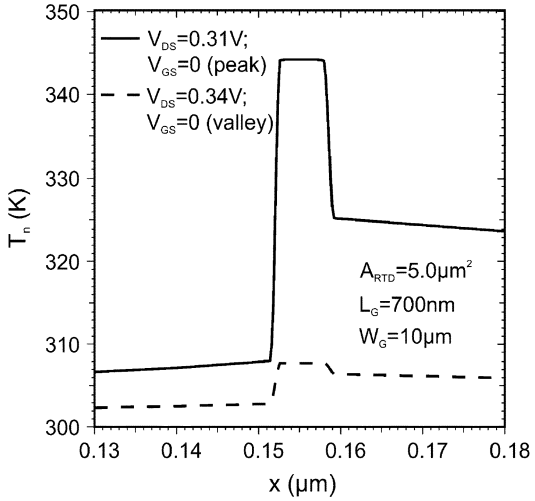

Fig. 6. Electron temperature distribution at $V_{\mathrm{DS,peak}}$ and $V_{\mathrm{DS,valley}}$ of the integrated RTD.

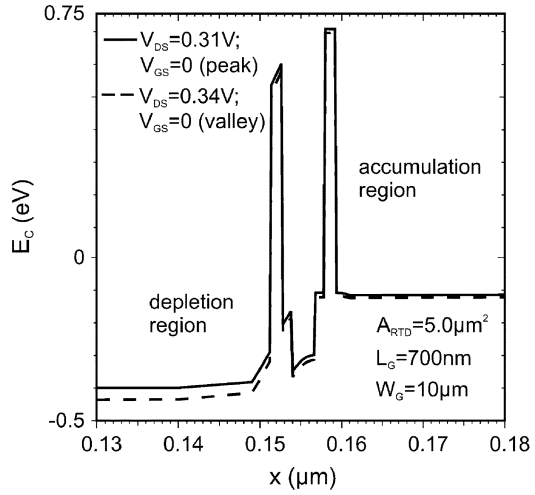

Fig. 7. Conduction band energy at $V_{\mathrm{DS,peak}}$ and $V_{\mathrm{DS,valley}}$ in the range of the integrated RTD.

barriers. For the integrated RTD the presence of significant charge accumulation cannot be indicated on the source side of the barrier during the valley current phase operation, like in most studies, where the tunneling process is concentrated to the first subband [21]. One reason is the main tunneling process to the second subband, which is connected to the highly doped contact regions. Secondly, the decrease of the electron density distribution in the accumulation region at the valley phase operation corresponds to the increase of the electron current in the channel region (I_{HEMT}), because the same source contact of the integrated device is used and the electrons cannot tunnel through the potential barriers. The continuous electron distribution is the consequence of the quantum correction term in the transport equation (11). The quantum correction in the quantum drift diffusion model or the so-called density gradient model provides a useful approach of the Schrödinger equation, which delivers the same results for the electron density distribution in the ranges where quantum mechanical effects are expected.

In Fig. 6 the electron temperature distribution is shown at different drain source voltages ($V_{\mathrm{DS,peak}}$ and $V_{\mathrm{DS,valley}}$) for the region of the integrated RTD only. For the bias point $V_{\mathrm{DS,peak}} = 0.31$ V an increasing electron temperature in the range of the two potential barriers is detected, which is an identifier for the tunneling process through the RTD. The electron temperature decreases at the bias point $V_{\mathrm{DS,valley}} = 0.34$ V in the range of the RTD. The gradient of the carrier temperature is included in the carrier transport equation (11). With the increase of the carrier temperature a higher current density is expected. With including the quantum energy balance equations in the quantum drift diffusion model, the modeling of tunneling processes through potential barriers is possible.

The conduction band edge of the RTD at $V_{\mathrm{DS,peak}} = 0.31$ V and $V_{\mathrm{DS,valley}} = 0.34$ V is represented in Fig. 7. The accumulation and the depletion region are shown. The additional quantum well between the two potential barriers allows that the first subband is occupied and the main tunneling process is concentrated to the second subband energy, whereas the tunneling peak in the output characteristics (Fig. 3) is shifted to lower bias points. The tunneling-current densities as well as the peak-to-valley ratios increase.

Fig. 8 shows the quantum correction potential in the range of the integrated RTD for the bias point $V_{\mathrm{DS,peak}} = 0.31$ V. At the different hetero interfaces strong discontinuities are recognized. The sum of the conduction band edge and the quantum correction potential delivers a continuous potential description. The exponential function of this potential is proportional to the continuous carrier density distribution. The strong discontinuities at the hetero interfaces require a high density of discretization points in these ranges to avoid numerical overflows and convergence problems. The convergence behavior of the Newton iteration of the quantum correction potential as well as the coupled system of equations of the quantum hydrodynamic model for the example of the monolithic integrated device is complicated.

C. Variations

Further investigations of some structure modifications were carried out. Especially the RTD area (A_{RTD}) and the gate width

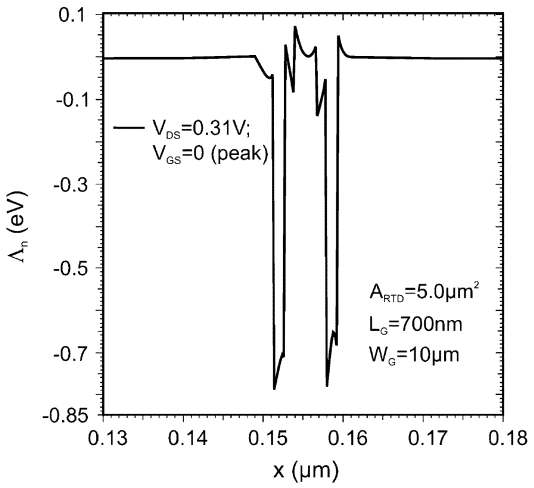

Fig. 8. Quantum correction potential at $V_{\mathrm{DS,peak}}$ in the range of the both potential barriers.

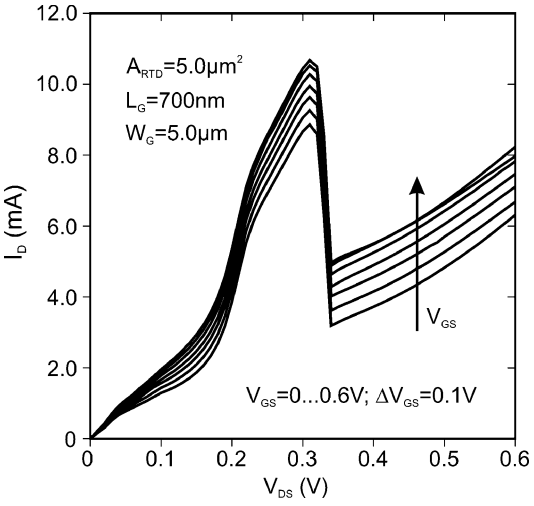

Fig. 9. Output characteristics of the RTD-HEMT for $A_{\mathrm{RTD}} = 5.0\ \mu\mathrm{m}^2$ and $W_G = 5.0\ \mu\mathrm{m}$.

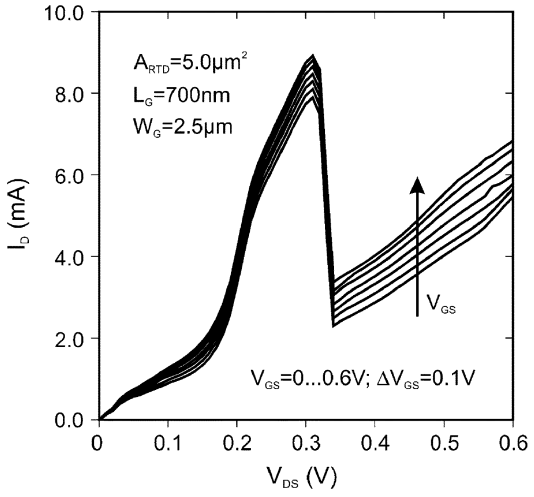

Fig. 10. Output characteristics of the RTD-HEMT for $A_{\mathrm{RTD}} = 5.0\ \mu\mathrm{m}^2$ and $W_G = 2.5\ \mu\mathrm{m}$.

(W_G) of the integrated HEMT vary. Figs. 9 and 10 show the output characteristics of the RTD-HEMT, in which the RTD has

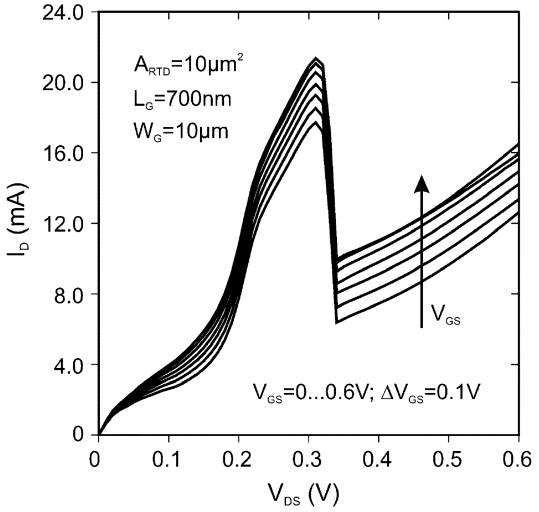

Fig. 11. Output characteristics of the RTD-HEMT for $A_{\mathrm{RTD}} = 10.0\ \mu\mathrm{m}^2$ and $W_G = 10.0\ \mu\mathrm{m}$.

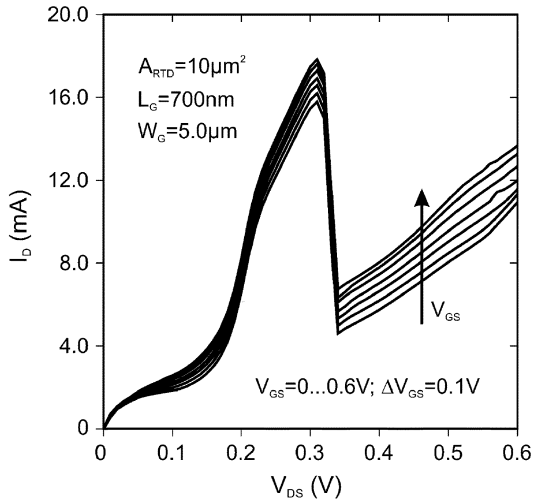

Fig. 12. Output characteristics of the RTD-HEMT for $A_{\mathrm{RTD}} = 10.0\ \mu\mathrm{m}^2$ and $W_G = 5.0\ \mu\mathrm{m}$.

an area of $A_{\mathrm{RTD}} = 5.0\ \mu\mathrm{m}^2$ and the HEMTs possess nominal gate widths of $W_G = 5.0\ \mu$m and $W_G = 2.5\ \mu$m. In Figs. 11 and 12, the output characteristics are represented for the same devices, but the RTD area is changed to $A_{\mathrm{RTD}} = 10.0\ \mu\mathrm{m}^2$ and the gate widths of the integrated HEMTs are doubled. As shown in Fig. 3 the total current of the integrated device is modulated by the gate voltage. Since the current of each HEMT is proportional to its gate width, the modulation amplitude of the total current for each gate should be proportional to the gate width. For the device, which has an integrated RTD with $A_{\mathrm{RTD}} = 5.0\ \mu\mathrm{m}^2$, the current modulation at the peak ($V_{\mathrm{DS,peak}} = 0.31$ V), with a variable bias voltage of $V_{\mathrm{DS}} = 0$ to $V_{\mathrm{DS}} = 0.6$ V, is $\Delta I_m = 1.03$ mA ($W_G = 2.5\ \mu$m, Fig. 10), $\Delta I_m = 1.82$ mA ($W_G = 5.0\ \mu$m, Fig. 9) and $\Delta I_m = 4.15$ mA ($W_G = 10.0\ \mu$m, Fig. 3). The current modulation ratio $(1.03 : 1.82 : 4.15 = 1 : 1.87 : 4.04)$ is not exactly the same as the nominal gate width ratio $(1 : 2 : 4)$. The reasons are numerical inaccuracies of the simulation results when scaling the single device. For the integrated devices, in which RTD with $A_{\mathrm{RTD}} = 10.0\ \mu\mathrm{m}^2$ is included, a current modulation ratio of

$0.98 : 2.05 : 3.63 = 1 : 2.1 : 3.7$ is detected (Fig. 11 for $W_G = 10.0\ \mu$m and Fig. 12 for $W_G = 5.0\ \mu$m). The variation of the RTD area from $A_{\mathrm{RTD}} = 5.0\ \mu\mathrm{m}^2$ to $A_{\mathrm{RTD}} = 10.0\ \mu\mathrm{m}^2$ delivers an increase of the total drain current with the factor two (see Figs. 9–12). The nominal current modulation ratio is almost similar for these cases.

V. Summary and Conclusion

The derivation of the quantum hydrodynamic transport model is described. With the new quantum hydrodynamic model, it is possible to take into account quantum mechanical effects in all directions of a complex nanoscale device. The multidimensional implementation of the quantum correction potential with a finite box method is obtained, where an additional quantum potential $\lambda_n(\boldsymbol{R}, t)$ into the nonlinear system of unknown variables is introduced.

Numerical 2-D-simulations of monolithic ICs of resonant tunneling structures and HEMTs based on $In_{0.53}Ga_{0.47}As$–$In_{0.52}Al_{0.48}As$–InP are carried out. The first reported simulation of a monolithic IC by using a quantum hydrodynamic model is demonstrated. The NDR of resonant tunneling structures can be used for circuit functions, while HEMTs can be used to build buffers between neighboring circuits. The superiority of InP-based material system, which is used for the simulated IC, is demonstrated in terms of high peak current density and high peak-to-valley ratio.

The structure variations exhibit a good correspondence between the current modulation ratio and the nominal gate width ratio as well as the increase of the total current by the extension of the RTD area.

Acknowledgment

The authors would like to thank Dr. A. Wettstein for useful discussions of the numerical aspects during the implementation of the quantum correction potential.

References

[1] F. Capasso, S. Sen, and F. Beltram, *Quantum-Effect Devices, High-Speed Semiconductor Devices*, S. M. Sze, Ed. New York: Wiley, 1990, p. 465.

[2] C. L. Gardner, "The quantum hydrodynamic model for semiconductor devices," *SIAM J. Appl. Math.*, vol. 54, no. 2, pp. 409–427, Apr. 1994.

[3] E. Wigner, "On the quantum correction for thermodynamic equilibrium,," *Phys. Rev.*, vol. 40, pp. 749–759, 1932.

[4] K. Bløtekjær, "Transport equations for electrons in two-valley semiconductors," *IEEE Trans. Electron Devices*, vol. ED-17, pp. 38–47, Jan. 1970.

[5] G. J. Iafrate, H. L. Grubin, and D. K. Ferry, "Utilization of quantum distribution function for ultra-submicron device transport," *J. de Phys.*, vol. C7, no. 10(42), pp. 307–312, Oct. 1981.

[6] D. Bohm, "A suggest interpretation of the quantum theory in terms of hidden variables," *Phys. Rev.*, vol. 85, pp. 166–193, 1952.

[7] G. Baccarani and M. R. Wordeman, "An investigation of steady-state velocity overshoot effects in Si and GaAs devices," *Solid State Electron.*, vol. 28, pp. 407–416, 1985.

[8] Z. Chen, "A finite element method for the quantum hydrodynamic model for semiconductor devices," *Comput. Math. Appl.*, vol. 31, pp. 17–26, 1996.

[9] Z. Chen, B. Cockburn, C. L. Gardner, and J. W. Jerome, "Quantum hydrodynamic simulation of hysteresis in the resonant tunneling diode," *J. Comput. Phys.*, vol. 117, pp. 274–280, Mar. 1995.

[10] S. Selberherr, *Analysis and Simulation of Semiconductor Devices*, Berlin, Germany: Springer-Verlag, 1984.

[11] W. Klix, SIMBA-User Manual. Online. Available: http://www.htw-dresden.de/~klix/simba/welcome.html.

[12] A. Wettstein, A. Schenk, and W. Fichtner, "Quantum device simulation with the density-gradient model on unstructured grids," *IEEE Trans. Electron Devices*, vol. 48, pp. 279–284, Feb. 2001.

[13] H. K. Gummel, "A self-consistent iterative scheme for one-dimensional steady state transistor calculations," *IEEE Trans. Electron Devices*, vol. ED-11, pp. 455–465, 1964.

[14] K. J. Chen, K. Maezawa, and M. Yamamoto, "InP-based high-performance monostable-bistable transition logic element (MOBILE): An intelligent logic gate featuring weighted-sum threshold operations," *Jpn. J. Appl. Phys.*, pt. 1, vol. 35, no. 2B, pp. 1172–1177, Feb. 1996.

[15] C. L. Gardner, "Resonant tunneling in the quantum hydrodynamic model," in *VLSI Syst. Des.*, vol. 3, 1995, pp. 201–210.

[16] C. L. Gardner and C. Ringhofer, "The Chapman-Enskog expansion and the quantum hydrodynamic model for semiconductor devices," in *VLSI Syst. Des.*, vol. 10, 2000, pp. 415–435.

[17] C. Pigorsch, W. Klix, and R. Stenzel, "Quantum wire splitting in nanostructures," *Microelectron. Eng.*, vol. 43–44, pp. 325–333, 1998.

[18] S. K. Ghosh and B. M. Deb, "Densities density-functionals and electron fluids," *Phys. Rep.*, vol. 92, no. 1, pp. 1–44, 1982.

[19] S. Sonego, "Interpretation of the hydrodynamical formalism of quantum mechanics," *Found. Phys.*, vol. 21, no. 10, pp. 1135–1181, 1991.

[20] T. Takabayasi, "Remarks on the formulation of quantum mechanics with classical pictures and on relations between linear scalar fields and hydrodynamic fields," *Prog. Theor. Phys.*, vol. 9, no. 3, pp. 187–222, Mar. 1953.

[21] J. Höntschel, R. Stenzel, and W. Klix, "Investigations of quantum transport phenomena in resonant tunneling structures by simulations with a novel quantum hydrodynamic transport model," in *Proc. ISCS*, Lausanne, 2002, to be published.

[22] M. G. Ancona and H. F. Tiersten, "Macroscopic physics of the silicon inversion layer," *Phys. Rev. B, Condens. Matter*, vol. 35, no. 15, pp. 7959–7965, May 1987.

[23] M. G. Ancona and G. J. Iafrate, "Quantum correction to the equation of state of an electron gas in a semiconductor," *Phys. Rev. B, Condens. Matter*, vol. 39, no. 13, pp. 9536–9540, May 1989.

[24] E. Mandelung, "Quantentheorie in hydrodynamischer form," *Z. Phys.*, vol. 40, pp. 322–326, 1927.

[25] I. Gasser, P. A. Markowich, D. Schmidt, and A. Unterreiter, "Macroscopic theory of charged quantum fluids," *Math. Prob. Semi. Phys.*, vol. 340, pp. 42–75, 1995.

[26] I. Gasser and P. A. Markowich, "Quantum hydrodynamics, derivation classical limit," *Quantum Transport in Ultrasmall Devices*, ser. NATO ASI series, series B, vol. 342, pp. 493–496, 1995.

[27] ——, "Quantum hydrodynamics, Wigner transform and the classical limit," *Asympt. Anal.*, vol. 14, pp. 97–116, 1997.

[28] I. Gasser and A. Jüngel, "The quantum hydrodynamic model for semiconductors in thermal equilibrium," *Z. Angew. Math. Phys.*, vol. 48, pp. 45–59, 1997.

[29] J. R. Zhou and D. K. Ferry, "Simulation of ultra-small GaAs MESFET using quantum moment equations," *IEEE Trans. Electron Devices*, vol. 39, pp. 473–478, Mar. 1992.

[30] ——, "Simulation of ultra-small GaAs MESFET using quantum moment equations-II: Velocity overshoot," *IEEE Trans. Electron Devices*, vol. 39, pp. 1793–1796, Aug. 1992.

[31] ——, "Modeling of quantum effects in ultrasmall HEMT Devices," *IEEE Trans. Electron Devices*, vol. 40, pp. 421–427, Feb. 1993.

[32] H. L. Grubin and J. P. Kreskovsky, "Quantum moment balance equations and resonant tunneling structures," *Solid State Electron.*, vol. 32, no. 12, pp. 1071–1075, 1989.

[33] R. Pinnau and A. Unterreiter, "The stationary current-voltage characteristics of quantum drift-diffusion model," in *SIAM J. Numer. Anal.*, vol. 37, 1999, pp. 211–245.

[34] A. Wettstein, "Quantum effects in MOS devices," *Series Microelectron.*, vol. 94, 2000.

[35] C. Rafferty, B. Biegel, Z. Yu, M. Ancona, J. Bude, and R. Dutton, "Multidimensional quantum effect simulation using a density-gradient model and script-level programming techniques," in *Proc. SISPAD*, Lueven, Belgium, 1998, pp. 137–140.

[36] H. Tsuchiya and T. Miyoshi, "Quantum transport modeling of ultrasmall semiconductor devices," *IEICE Trans. Electron.*, vol. E82-C, no. 6, pp. 880–888, June 1999.

[37] Z. Yu, R. Dutton, and R. Kiehl, "Circuit/device modeling at the quantum level," in *Proc. Int. Workshop on Computational Electronics*, Osaka, Japan, 1998, pp. 222–229.

[38] A. Arnold, J. Lopez, and P. A. Markowich, An analysis of quantum Fokker-Planck models: A Wigner function approach, Preprint, TU Berlin, Germany, 1999.
[39] N. Kluksdahl, A. Kriman, D. K. Ferry, and C. Ringhofer, "Self-consistent study of the resonant tunneling diode," *Phys. Rev. B, Condens. Matter*, vol. 39, pp. 7720–7735, 1989.
[40] W. Frensley, "Simulation of resonant tunneling heterostructure devices," *J. Vacuum. Sci. Tech. B, Microelectron. Process. Phenom.*, vol. 3, pp. 1261–1266, 1985.

Jan Höntschel received the Dipl.-Ing. degree in electrical engineering in 2000 from the University of Applied Sciences Dresden, Germany, where he is pursuing the Ph.D. degree.

His current research interests include the simulation of quantum-sized devices and III–V semiconductor structures as well as the modeling of quantum transport phenomena in nanoscale devices.

Mr. Höntschel is a member of the German Association for Electrical, Electronic and Information Technologies (VDE) and was a recipient of the 2000 VDE award for an excellent diploma thesis.

Roland Stenzel (M'95) received the Dipl.-Ing. degree in electrical engineering, the Dr.-Ing. degree, and the habilitation degree from the Dresden University of Technology, Dresden, Germany, in 1979, 1983, and 1989, respectively.

From 1979 to 1989, he was with the Institute of Electron Devices and Systems, Dresden University of Technology, where he was engaged in the design and the numerical analysis of GaAs circuits and devices. From 1989 to 1990, he was with the GaAs Division, Institute of Electron Physics, German Academy of Sciences, Berlin, Germany, where he worked on a GaAs-MESFET design for application in digital ICs. From 1990 to 1992, he was a Professor of Theoretical Electrical Engineering at the University of Transportation, Dresden, and since 1992, he has been with the University of Applied Sciences Dresden, as a Professor of Theoretical Electrical Engineering and Semiconductor Devices. His current research interests include numerical simulation of HFETs and HBTs as well as novel quantum devices and SOI-MOSFETs.

Dr. Stenzel is a member of the German Association for Electrical, Electronic and Information Technologies.

Wilfried Klix received the Dipl.-Ing. degree in electrical engineering, and the Dr.-Ing. degree from the Dresden University of Technology, Dresden, Germany, in 1979 and 1987, respectively.

From 1979 to 2002, he was with the Institute of Electron Devices and Systems, Dresden University of Technology, where he was engaged in the design and the numerical analysis of semiconductor devices. Since 2002, he has been a Professor of Theoretical Electrical Engineering and Optoelectronics at the University of Applied Sciences Dresden. His currents research interests include numerical methods for the simulation of semiconductor devices as well as numerical simulation of SOI-MOSFETs and HFETs.